Aeroacoustics Conferences
June 4-7, 2024, Rome, Italy
30th AIAA/CEAS Aeroacoustics Conference (2024)

10.2514/6.2024-3205

Localized resolvent-mode bases for turbulence statistics

Ethan Eichberger * Liam Heidt † and Tim Colonius ‡
California Institute of Technology, Pasadena, CA USA

Modes from global resolvent analyses have been shown to accurately model the frequencies and spatial structure of the dominant coherent structures in several turbulent flows. However, resolvent-mode forcing models must be developed to predict the amplitude of the structures or other flow statistics, including the radiated noise. The present research aims to apply data-driven approaches to learn forcing coefficients from lower-order statistics available from Reynolds-averaged Navier-Stokes (RANS) predictions. As a first step towards this goal, we present a novel localized resolvent framework that reconstructs global quantities at low rank through spatially restricting the resolvent forcing and response domains. To illustrate the flexibility and robustness of the proposed framework, we initially utilize localized resolvent modes to reconstruct the spectral proper orthogonal decomposition (SPOD) modes of an isothermal Mach 0.4 jet at $Re = 450,000$. The results showcase the flexibility localized resolvent modes provide in the construction of global SPOD, while using 10 or fewer total localized modes total across $St = [0.05, 1.00]$. Furthermore, we employ localized resolvent modes to reconstruct second-order statistics, comparing their performance with that of global modes. At low reconstruction error, it is shown that about twice as many global modes are needed to achieve comparable errors.

I. Introduction

Coherent structures play a crucial role in the dynamics and acoustics of turbulent jets. Their identification from data using spectral proper orthogonal decomposition (SPOD) [1] and their modeling using resolvent analysis [2] have improved our understanding of these flows [3–7].

Resolvent analysis identifies the optimal forcing and response modes with the largest gain based on a linearization of the governing equations about the turbulent mean flow [2]. The framework bears resemblance to the acoustic analogy [8], and more specifically its generalization [9], wherein the predicted flow or acoustic field are governed by a linear operator driven by nonlinear products of fluctuations, regarded as equivalent sources of the resulting motions/waves. The resolvent differs from the traditional approach by replacing the Green's function solution with a decomposition of the operator into a set of orthonormal modes ordered by the *gain* between the forcing and response. Compare to traditional acoustic analogy, this potentially lowers the modeling burden to the forcing coefficients of a few modes. This approach has already enjoyed some success in jet noise modeling[7, 10–13].

Resolvent modes are likewise capable of predicting the structure of the near-field coherent vortical motions [2–4, 14], but, as for the far field, models for the sources are required to predict their amplitudes. While several data-driven approaches have been proposed to estimate the sources from data [15–17], fully predictive frameworks have not yet been established. In this research, we aim to develop resolvent forcing models that are informed by mean-flow quantities that can reliably be predicted in RANS, ultimately in order to develop RANS-based jet-noise models. We are particularly interested in resolvent modes that simultaneous capture near and far-field behaviors, so that solely near-field quantities can be used as inputs to determine their magnitude.

However, a challenge stems from the nature of global modes, which span the entire spatial flow. In many flows, the coherent structures differ in structure and frequency in different regions of the flow. For example, a turbulent jet has a spatial domain that includes the near nozzle flow, the annular shear layer, the end of the potential core, the fully-developed jet (with an increasingly thick shear layer), and the near and far acoustic fields. By focusing solely on the global jet behavior, these modes are, at low rank, likely to be only weakly correlated with corresponding statistics available from RANS.

To address this challenge, in this paper we develop what we term as a *localized resolvent basis* that computes modes whose forcing and observation regions are broken down into a set of possibly overlapping spatial regions, while retaining

*PhD Student, Mechanical and Civil Engineering, AIAA Student Member
†PhD Candidate, Graduate Aerospace Laboratories of the California Institute of Technology, AIAA Student Member
‡Frank and Ora Lee Marble Professor of Mechanical Engineering, Mechanical and Civil Engineering, Associate Fellow AIAA

the global definition of the flow state. This adds flexibility and robustness to the construction of global solutions. In section II, we start by outlining the procedure used to reconstruct desired outputs using the localized resolvent bases. To showcase localized resolvent analysis, localized resolvent modes are first used to optimally reconstruct global SPOD modes of an isothermal turbulent jet presented in section III.A. Additionally, in section III.B, localized and global resolvent modes are used to model second-order statistics. For this paper, the turbulent kinetic energy (TKE) and Reynolds stresses of an isothermal turbulent jet are reconstructed; future work will extend this to the acoustic field.

II. Methodology

A brief overview of resolvent analysis and SPOD is presented to provide the necessary information to introduce the localized resolvent approach. The reader is referred to Lumley [1], McKeon and Sharma [2], Towne et al. [5] for details.

A. Resolvent analysis

Resolvent analysis predicts coherent structures in turbulent flows by finding the highly linearly amplified fluctuations to a given time-invariant mean flow [2]. We begin with the linearized compressible Navier-Stokes equations written in the frequency domain

$$(i\omega \boldsymbol{I} - \boldsymbol{A}_m)\hat{\boldsymbol{q}}_{m,\omega} = \boldsymbol{B}\hat{\boldsymbol{f}}_{m,\omega}, \tag{1a}$$

$$\hat{\boldsymbol{y}}_{m,\omega} = \boldsymbol{C}\hat{\boldsymbol{q}}_{m,\omega}, \tag{1b}$$

where $\boldsymbol{q} = [\boldsymbol{\rho}', \boldsymbol{u}_r', \boldsymbol{u}_\theta', \boldsymbol{u}_x', \boldsymbol{T}']^T$ is a state vector comprised of the fluctuating flow quantities (departures from the mean) discretized in the x and r directions, and $\hat{\boldsymbol{q}}_{m,\omega}$ is its Fourier transform in time and azimuth; ω is the temporal frequency, and m is the azimuthal mode number. The forcing, $\hat{\boldsymbol{f}}_{m,\omega}$, is the collection of all nonlinear terms. Additionally, the $\boldsymbol{B}$ and $\boldsymbol{C}$ matrices are the forcing and response spatial domain restrictions, respectively. This results in $\hat{\boldsymbol{y}}_{m,\omega}$ being the spatially restricted response or observation. The relationship between the forcing and observation is expressed through combining equations (1a) and (1b),

$$\hat{\boldsymbol{y}}_{m,\omega} = \boldsymbol{C}\boldsymbol{R}\boldsymbol{B}\hat{\boldsymbol{f}}_{m,\omega}, \tag{2}$$

$$\boldsymbol{R}_{m,\omega} = (i\omega \boldsymbol{I} - \boldsymbol{A}_m)^{-1}, \tag{3}$$

where $\boldsymbol{R}_{m,\omega}$ is defined as the resolvent operator. Thus, the resolvent operator acts as the transfer function between the forcing, $\boldsymbol{f}_{m,\omega}$ and the observation, $\boldsymbol{y}_{m,\omega}$. The goal of resolvent analysis is to find the optimal forcing and response pairs, at each frequency and azimuthal mode number, that maximizes their linear gain

$$\sigma^2 = \max_{\hat{f}} \frac{\hat{\boldsymbol{y}}^H_{m,\omega}\boldsymbol{W}_y\hat{\boldsymbol{y}}_{m,\omega}}{\hat{\boldsymbol{f}}^H_{m,\omega}\boldsymbol{W}_f\hat{\boldsymbol{f}}_{m,\omega}} = \max_{\hat{f}} \frac{\hat{\boldsymbol{f}}^H_{m,\omega}\boldsymbol{B}^H\boldsymbol{R}^H_{m,\omega}\boldsymbol{C}^H\boldsymbol{W}_y\boldsymbol{C}\boldsymbol{R}_{m,\omega}\boldsymbol{B}\hat{\boldsymbol{f}}_{m,\omega}}{\hat{\boldsymbol{f}}^H_{m,\omega}\boldsymbol{W}_f\hat{\boldsymbol{f}}_{m,\omega}} \tag{4}$$

with σ denoting the linear gain and ^{H} is the hermitian transpose. As in previous studies of turbulent jets [3, 4, 10, 11], we employ the Chu compressible energy norm [18] for both the forcing and response, $\boldsymbol{W}_f$ and $\boldsymbol{W}_y$. The optimization problem in (4) is solved by computing the singular value decomposition (SVD) of

$$\boldsymbol{H}_{m,\omega} = \boldsymbol{W}_y^{\frac{1}{2}}\boldsymbol{C}\boldsymbol{R}_{m,\omega}\boldsymbol{B}\boldsymbol{W}_f^{-\frac{1}{2}} = \boldsymbol{U}^\dagger_{m,\omega}\boldsymbol{\Sigma}_{m,\omega}\boldsymbol{V}^{\dagger\boldsymbol{H}}_{m,\omega} \tag{5}$$

where $\boldsymbol{V}_{m,\omega} = \boldsymbol{W}_f^{-1/2}\boldsymbol{V}^\dagger_{m,\omega}$ and $\boldsymbol{U}_{m,\omega} = \boldsymbol{W}_y^{1/2}\boldsymbol{U}^\dagger_{m,\omega}$ are the forcing and responses modes at a specific frequency and azimuthal wave number ranked with respect to their linear gain, $\boldsymbol{\Sigma}_{m,\omega}$.

We employ the RANS-based eddy-viscosity method of Pickering et al. [4] as the baseline for the global resolvent analysis. This method improved the alignment between dominant global resolvent modes and SPOD modes over all relevant frequencies and azimuthal mode numbers. Similar to Pickering et al. [4], a scale constant of $c = 1/7$ is employed for all cases. This is similar to previous studies performed by [4, 19] and is determined to give good alignment over the range of frequencies of interest.

B. Localized resolvent analysis

We define our localized resolvent modes as $\hat{\boldsymbol{q}}^{(i,j,g)}_{m,\omega}$ where i and j denotes the i^{th} forcing and j^{th} observation (output) locations, and g is the corresponding mode number. Note that the response, $\hat{\boldsymbol{q}}^{(i,j,g)}_{m,\omega}$, remains global–it is only the

observation and forcing spaces that are restricted. It is not the domain that has been changed by localization, but the measure of *gain* between input and output–these modes characterize the gain between restricted regions, but are defined globally.

The forcing and response regions are defined by smooth weightings that we determine using splines. While we could consider any arbitrary decomposition of the domain into local regions, we choose regions that span the axial length of the computational domain, as shown in figure 1. The spline knots, the points between each consecutive spline, are uniform over the computational domain. Eventually, we may consider optimizing the decomposition of the domain. Note that uniform knots produce regions of varying size. The specific localization depicted in figure 1 divides the computational domain of the jet into 6 local regions, which is the case exclusively considered in this paper to represent the Mach 0.4 jet we discuss below.

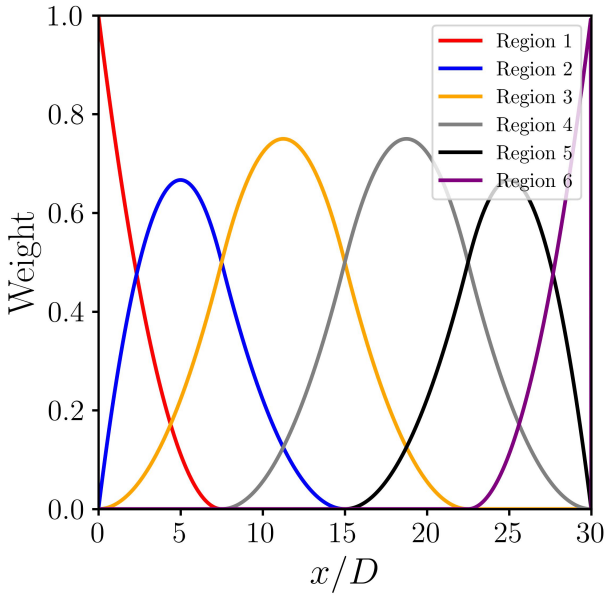

Fig. 1 Resolvent forcing and response localized domains. Splines used to define the axial weight of each local region

To demonstrate the motivation for localized resolvent analysis, we present localized forcing and response modes of an isothermal Mach 0.4 round jet at $Re = 450,000$. The temporal frequency is reported as the Strouhal number, $St = \omega/(2\pi M_j)$, where ω is the non-dimensional temporal frequency and M_j is the Mach number of the jet. In figure 2, we display the radial velocity component of the dominant resolvent modes at $m = 0$ and $St = 0.20$. The restricted forcing and observation domains of the localized resolvent modes are outlined by the white dashed lines. As a reference, the global forcing and response modes are also shown. From the global resolvent mode, we notice that the forcing has the highest intensity near the nozzle of the jet. We see the response of the global forcing is dominated by forcing near the nozzle by comparing it to the first 2 localized modes where the forcing is restricted to $x/D = [0, 5]$. These response modes are similar, even when downstream forcing elements present in the global resolvent forcing are absent. This is further evidenced by looking at the responses of localized modes 1 and 2. Despite the two separate observation domains, the response modes yield nearly identical results. As the forcing restriction is moved downstream, the initial growth of the response structures moves in parallel, where the initial growth begins downstream of the initial forcing.

Thus, decomposing the forcing/response modes into multiple localized regions allows for the spatially dependent physics (and thus optimal amplification mechanisms) to be captured without the modes being dominated by the globally most amplified structures. This is analogous to how restricted versions of SPOD [3] have been performed to isolate the most energetic low-frequency structures in the near-nozzle region rather than the global modes being dominated by energy low-frequency components further downstream. This phenomenon plays a pivotal role in reconstructing the desired outputs throughout the paper. The importance and effect of using these localized forcing and observation regions will be explored more in section III.A.

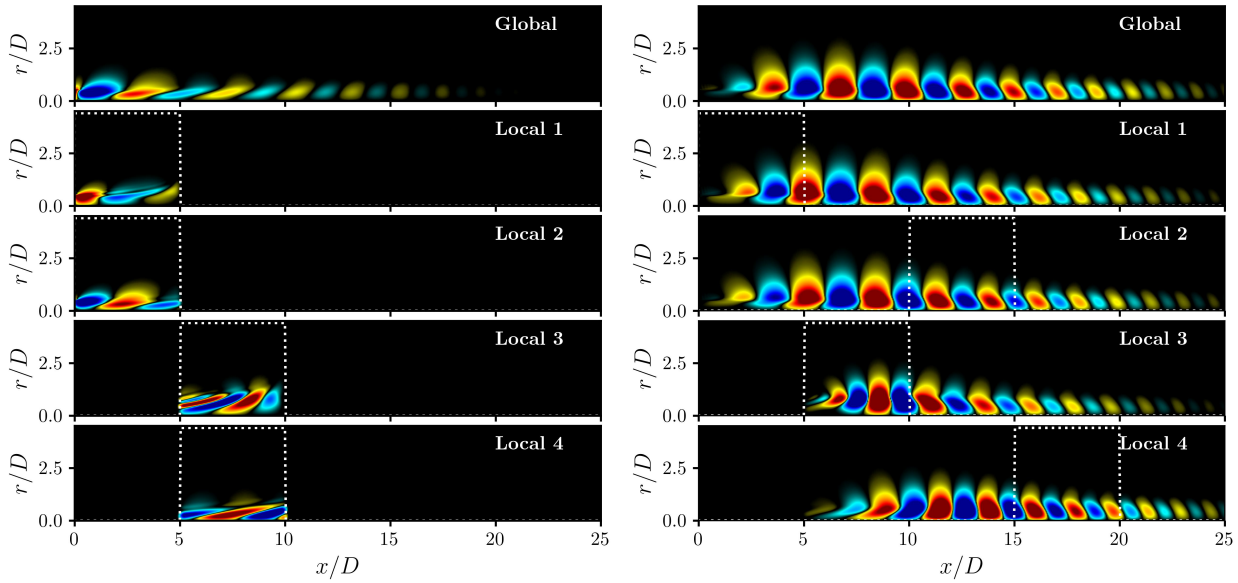

(a) Global and localized forcing modes **(b) Global and localized response modes**

Fig. 2 Effect of localized forcing and output on the response mode compared to global resolvent. Outlined in the white dashed line is the axial weight of the local region.

C. Spectral proper orthogonal decomposition

Spectral proper orthogonal decomposition (SPOD) [1] determines the optimal orthogonal basis of flow data that is ranked in terms of total energy captured. SPOD modes vary in both space and time, which provides both the spatial and temporal correlation in the data. To computed SPOD modes, the LES data is represented as the collection of all snapshots, $\boldsymbol{Q} = [\boldsymbol{q}_1, \boldsymbol{q}_2, \ldots, \boldsymbol{q}_M]$. To estimate the cross-spectral density (CSD) tensor, $\boldsymbol{Q}$ is decomposed into separate blocks to obtain the convergent estimates through Welch's [20] method. Next, the discrete Fourier transform (DFT) of each block is computed and the blocks are rearranged according to frequency, $\hat{\boldsymbol{Q}}_f$. The CSD tensor is estimated at frequency f by

$$\boldsymbol{S}_f = \hat{\boldsymbol{Q}}_f \hat{\boldsymbol{Q}}_f^H. \tag{6}$$

Thus, we can solve for the SPOD modes through the matrix eigenvalue problem,

$$\boldsymbol{S}_f \boldsymbol{W} \boldsymbol{\Psi}_f = \boldsymbol{\Psi}_f \boldsymbol{\Lambda}_f \tag{7}$$

where $\boldsymbol{W}$ is again the Chu compressible energy norm. In this paper, we used a total of 20,000 snapshots with a frequency bin width $\Delta St = 0.05$ for Strouhal number (St) $St > 0.1$ and $\Delta St = 0.025$ for all other frequencies. We refer the reader to Heidt and Colonius [21] for the importance of using the correct frequency bin width when computing SPOD modes.

D. Reconstruction of SPOD modes

SPOD modes are reconstructed via a linear combination of the localized resolvent response modes

$$\boldsymbol{U}_{m,\omega}^{(g)} = \sum_{k=1}^{N_k} \sum_{i=1}^{N_B} \sum_{j=1}^{N_C} \hat{\boldsymbol{q}}_{m,\omega}^{(i,j,k)} \alpha_{i,j,k}, \tag{8}$$

where $\boldsymbol{U}_{m,\omega}^{(g)}$ is the reconstructed SPOD mode, N_B, N_C is the number of forcing and response regions, N_k is the number of subdominant localized modes employed, and g denotes the global mode number being reconstructed. Thus, we can express all localized modes as one matrix,

$$\boldsymbol{U}_{m,\omega}^{Local} = [\hat{\boldsymbol{q}}_{m,\omega}^{(1,1,1)}, \hat{\boldsymbol{q}}_{m,\omega}^{(1,2,1)}, \ldots, \hat{\boldsymbol{q}}_{m,\omega}^{(N_B,N_C,N_\sigma)}]. \tag{9}$$

and equation (8) is equivalently expressed as

$$\boldsymbol{U}^{(g)}_{m,\omega} = \boldsymbol{U}^{Local}_{m,\omega}\boldsymbol{\alpha}_{m,\omega}. \tag{10}$$

The coefficient $\boldsymbol{\alpha}$ is then solved using LASSO regression, which is through the minimization of the cost function

$$\mathcal{J} = \|\boldsymbol{\Psi}^{(g)}_{m,\omega} - \boldsymbol{U}^{Local}_{m,\omega}\boldsymbol{\alpha}_{m,\omega}\|^2_{\boldsymbol{W}} + \lambda_\ell \|\boldsymbol{\alpha}_{m,\omega}\|_1, \tag{11}$$

where $\boldsymbol{\Psi}$ is the desired SPOD mode, and λ_ℓ controls the penalization that controls the number of modes used in the reconstruction.

E. Reconstruction of flow statistics

In addition, we examine the extent to which the localized resolvent basis is efficient and robust at reconstructing flow statistics (and eventually the far-field sound). All second-order statics of the fluctuating state variables are contained in a covariance matrix, defined in real space by

$$\boldsymbol{\Phi}(\tau, \Delta\theta) = \mathbf{E}[\boldsymbol{q}(t,\theta)\boldsymbol{q}^T(t+\tau, \theta+\Delta\theta)] \tag{12}$$

where, as we are dealing with discretized flow quantities, the block-diagonal entries represent self- and cross-correlations between quantities at the same point, and off-diagonal entries represent self- and cross-correlations between quantities at different points. Owing to stationarity and homogeneity, the covariance only depends on the time and azimuthal shifts, τ and $\Delta\theta$, respectively. Likewise, the expectation can be represented as an integral over θ and t:

$$\boldsymbol{\Phi}(\tau, \Delta\theta) = \frac{1}{4T\pi}\int_{-T}^{T}\int_{0}^{2\pi} \boldsymbol{q}(t,\theta)\boldsymbol{q}^T(t+\tau,\theta+\Delta\theta)d\theta dt, \tag{13}$$

where T is a sufficiently long time. As we are interested in reconstructing the covariance at $\tau = \Delta\theta = 0$, we obtain, after inserting the Fourier transform on the right-hand side,

$$\begin{aligned}
\boldsymbol{\Phi}(0,0) &= \frac{1}{4T\pi}\int_{-T}^{T}\int_{0}^{2\pi} \sum_{\omega}\sum_{\omega'}\sum_{m}\sum_{m'} \hat{\boldsymbol{q}}_{m,\omega}\hat{\boldsymbol{q}}^H_{m,\omega} e^{i\omega t} e^{im\theta} e^{i\omega' t} e^{im'\theta} d\theta dt, \\
&= \frac{1}{4T\pi}\int_{-T}^{T}\int_{0}^{2\pi} \sum_{\omega}\sum_{\omega'}\sum_{m}\sum_{m'} \hat{\boldsymbol{q}}_{m,\omega}\hat{\boldsymbol{q}}^H_{m,\omega} e^{i\omega t} e^{im\theta} e^{i\omega' t} e^{im'\theta} d\theta dt, \\
&= \sum_{m}\sum_{\omega} \hat{\boldsymbol{q}}_{m,\omega}\hat{\boldsymbol{q}}^H_{-m,-\omega},
\end{aligned} \tag{14}$$

where we invoked orthogonality in arriving at the last line. In what follows we suppress the $(0,0)$ argument on $\boldsymbol{\Phi}$.

We represent $\hat{\boldsymbol{q}}_{\omega,m}$ as a linear combination of the response to each localized resolvent mode

$$\hat{\boldsymbol{q}}_{m,\omega} = \sum_i \boldsymbol{U}^{(i)}_{m,\omega}\boldsymbol{\Sigma}^{(i)}_{m,\omega}\boldsymbol{V}^{(i)H}_{m,\omega}\boldsymbol{W}\boldsymbol{B}^{(i)}\hat{\boldsymbol{f}}^{(i)}_{m,\omega}, \tag{15}$$

where i now denotes a specific localized forcing and response *pair*. The expanded form becomes

$$\boldsymbol{\Phi} = \sum_{\omega,m}\sum_{i,j} \boldsymbol{U}^{(i)}_{m,\omega}\boldsymbol{\Sigma}^{(i)}\boldsymbol{V}^{H(i)}\boldsymbol{W}\boldsymbol{B}^{(i)}\boldsymbol{S}^{(i)}_{ff}\boldsymbol{B}^{H(i)}\boldsymbol{W}\boldsymbol{V}^{(i)}\boldsymbol{\Sigma}^{H(i)}\boldsymbol{U}^{H(i)}_{-m,-\omega}. \tag{16}$$

where we denote $\boldsymbol{S}^{(i)}_{ff} = \hat{\boldsymbol{f}}^{(i)}\hat{\boldsymbol{f}}^{H(i)}$, the cross-spectral density of the forcing coefficients. Imposing that, statistically, the modes with (ω, m) are the same as those with $(-\omega, -m)$, we can define

$$\boldsymbol{F}^{(i)}_{m,\omega} = \boldsymbol{\Sigma}^{(i)}\boldsymbol{V}^{H(i)}\boldsymbol{W}\boldsymbol{B}^{(i)}\boldsymbol{S}^{(i)}_{ff}\boldsymbol{B}^{H(i)}\boldsymbol{W}\boldsymbol{V}^{(i)}\boldsymbol{\Sigma}^{H(i)}, \tag{17}$$

so that equation (16) may be written as

$$\boldsymbol{\Phi} = \sum_{\omega,m}\sum_{i} \boldsymbol{U}^{(i)}_{m,\omega}\boldsymbol{F}^{(i)}_{m,\omega}\boldsymbol{U}^{H(i)}_{m,\omega}. \tag{18}$$

Thus, we have arrived at the exact representation of the statistics. To reduce the order of the model, the resolvent basis is truncated to the first G dominant modes, and the frequency and azimuthal wavenumbers are truncated to $\omega = [-\Omega, \Omega]$ and $m = [-M, M]$. The estimated covariance tensor using the truncated resolvent basis is thus

$$\tilde{\boldsymbol{\Phi}} = \sum_{-\Omega}^{\Omega} \sum_{-M}^{M} \sum_{i}^{N_\ell} \tilde{\boldsymbol{U}}^{(i)}_{m,\omega} \tilde{\boldsymbol{F}}^{(i)}_{m,\omega} \tilde{\boldsymbol{U}}^{*(i)}_{m,\omega}, \tag{19}$$

where the $\tilde{(\cdot)}$ represents quantities that have been truncated to the first G modes and $N_\ell = N_C \times N_B$. Note that an equivalent expression for global, rather than localized modes, is obtained by removing the sum over the localization (removing the i sum).

III. Results

A. Reconstruction of SPOD modes

The SPOD modes are computed from an experimentally verified large-eddy simulation of the subsonic jet detailed in section II.B, using the "CharLES" compressible flow solver by Cascade Technologies[22–24], now part of Cadence Design Systems.

To compute the localized resolvent modes, the forcing/response regions are partitioned as specified in section II.B. Each mode reconstruction uses the 3 highest-gain localized resolvent modes per forcing and response region pairs, resulting in a maximum of 108 localized modes that are available during the optimization. To accurately compute the high-frequency resolvent modes, without introducing numerical/artificial modes, a more restricted domain is employed with increasing frequency. Thus, the number of localized modes available for each reconstruction is dependent on the Strouhal number since, for all cases, the same spline regions are employed. To compare the accuracy of the reconstruction, the alignment or projection of the resolvent mode onto the SPOD mode is computed, where a value of 1 means the modes are equivalent and orthogonal when 0. Alignment is calculated by computing the inner-product between the two modes with respect to the Chu compressible energy norm.

We first present the reconstruction of the $m = 0$ SPOD modes at $St = 0.20$ and $St = 0.60$ in figure 3 and 4. We compare the radial velocity component of the two most optimal SPOD modes at each frequency to three different resolvent-based methods. We first compute the response mode using the global resolvent analysis, which serves as a baseline. Two separate optimization methods were then used in the mode reconstruction. The first was computed using LASSO regression to provide a comparison between the number of modes used and the accuracy of the computed modes. The next optimization uses least squares minimization (equal to LASSO regression with $\lambda_\ell = 0$), which uses 75 total localized modes since the domain only spans 5 out of the 6 localized regions, $x = [0, 22.5]$. This acts as the ceiling of the mode reconstruction and aids in the analysis of the LASSO regression.

For $St = 0.20$, we see that using just 4 localized modes results in a $\approx$ 20% increase in the alignment of the reconstruction of the dominant mode displayed in figure 3a. Predominately, we see the localized approach can accurately capture the initial growth of the structures downstream of the nozzle. In contrast, global resolvent predicts that these structures begin closer to the nozzle. The main improvement with the addition of more localized modes is the ability to better capture the initial (near nozzle) development of these structures. In addition, the downstream statistical noise found in the SPOD modes is also captured with a sufficient number of localized modes. Turning our attention to the subdominant mode reconstruction in figure 3b, global resolvent captures double-wavepacket structures in the SPOD response but is unable to model their spatial location accurately. Localized resolvent analysis enhances the spatial modeling of these complex structures with just 10 localized modes, improving the alignment by over 35%.

To determine the trade-off between the number of localized modes and the accuracy of alignment, in figure 5, we show how each additional localized mode affects the reconstruction alignment. At $St = 0.20$, the first few additional localized modes substantially enhance the alignment for both modes 1 and 2. After approximately 20 localized modes, the alignment improvement decreases with each additional mode, and the reconstructed mode starts to overfit the data by modeling the noise.

At a higher frequency of $St = 0.60$, the dominant global mode already predicts the SPOD mode with high accuracy due to the low-rankness present at this frequency as documented in previous studies [4, 5]. Consequently, the localized resolvent reconstruction offers a marginal enhancement, primarily by modeling the statistical noise inherent in the SPOD mode. For the subdominant mode, global resolvent captures the spatial location of the double-wavepacket in the SPOD mode well. Similar to the $St = 0.20$ subdominant modes, the alignment increases dramatically by 25% with just

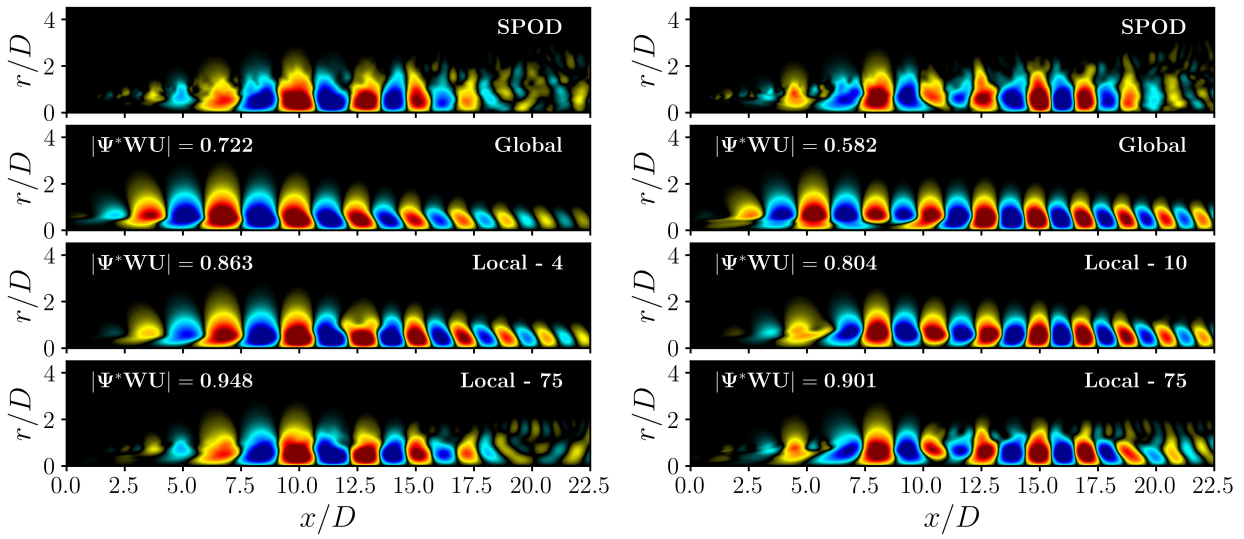

(a) Mode 1 **(b) Mode 2**

Fig. 3 Comparison of global and localized resolvent reconstruction of the two most dominant SPOD modes at $St = 0.20$, $m = 0$. The radial velocity perturbation component is shown with contour limits corresponding to $\pm 0.5|\psi_{u_r}|_\infty$. For each resolvent mode, the number of modes used is denoted in the top right of the plot, and the alignment, $|\Psi^H WU|$, is displayed in the top left corner.

7 localized modes due to the low statistical convergence of the subdominant modes, which stems from the small energy separation between the second and third most energetic modes. This small energy separation results in the third most dominant mode imprinting onto the second mode. Since the localized mode reconstruction employs the first three most amplified structures, it is able to capture this imprinting well, thereby substantially improving the reconstruction. As shown in figure 3b, additional localized modes extend beyond modeling the general mode shape and begin reproducing the nonphysical statistical noise. Thus, the implementation of LASSO regression assists in preventing this overfitting.

Figure 5b illustrates the transition from modeling the physical to nonphysical quantities by plotting the number of localized modes versus alignment. For the dominant mode, a slight increase of alignment is shown only for the first 5 localized modes due to the already accurate prediction by global resolvent. In contrast, the subdominant mode exhibits a substantial increase in mode alignment with a small number of localized modes, while additional modes beyond 10 offer diminishing improvements and primarily begin to model the statistical noise.

To better understand the effects of localized forcing and response resolvent modes, in figure 6 we look at the three localized modes with the highest absolute amplification coefficient for the reconstructions. Each localized plot displays the axial weight of the computational domain described in figure 1 to visualize the local region of the forcing and response modes denoted by a white dashed line. First, we look at the localized reconstruction of the most dominant mode found in figure 3a. When compared to the SPOD mode, the global resolvent response predicts the initial growth of the coherent structure more near the nozzle than the SPOD mode. This response arises from a dominant forcing effect near the nozzle. Regarding the localized modes, the three most amplified responses consist of two locally dominant and one subdominant mode. The most amplified localized mode yields a response where the initial growth is further downstream of the nozzle which the global response is unable to predict. This was achieved by reducing the forcing weight near the nozzle exit and focusing the response further downstream, thereby suppressing the dominant global structures excited in the near-nozzle region. The second localized mode has a shift in the localized forcing region downstream and an observation region upstream relative to the most amplified localized mode. The result is a response that helps capture the downstream effects of the SPOD mode and the irregular mode shape that happens at approximately $x/D = 12$. Lastly, the third localized mode, which is the subdominant mode of the most amplified response (Local 1), produces a response that assists in seeming together the first two localized modes and controls the amplitude of the mode in the energetic $x = [5, 15]$ region.

As for the subdominant reconstruction displayed in figure 3b, the global response once again has a premature initial

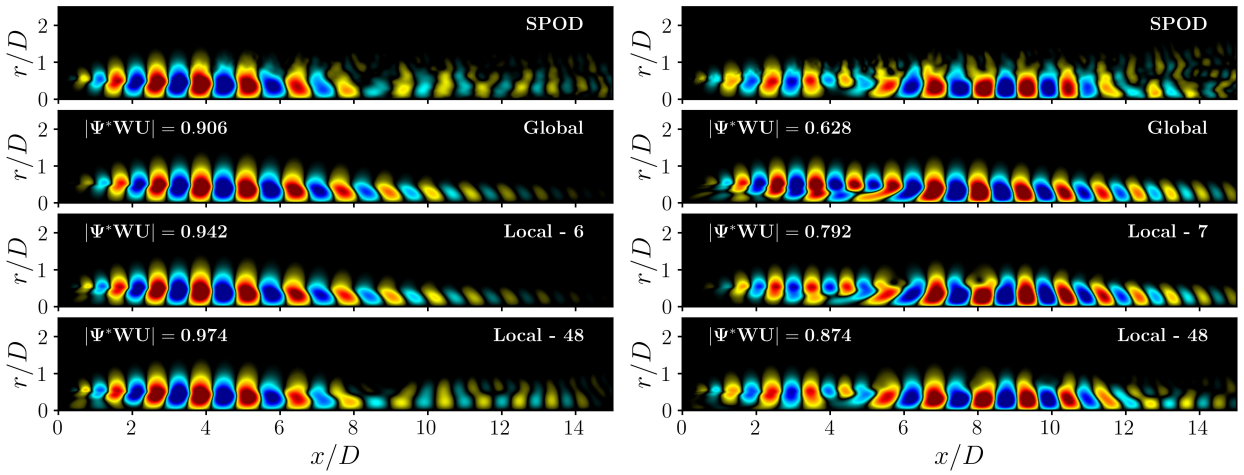

(a) Mode 1 **(b) Mode 2**

Fig. 4 Comparison of global and localized resolvent reconstruction of the two most dominant SPOD modes at $St = 0.60$, $m = 0$. The radial velocity perturbation component is shown with contour limits corresponding to $\pm 0.5|\psi_{u_r}|_\infty$. For each resolvent mode, the number of modes used is denoted in the top right of the plot, and the alignment, $|\Psi^H \mathbf{WU}|$, is displayed in the top left corner.

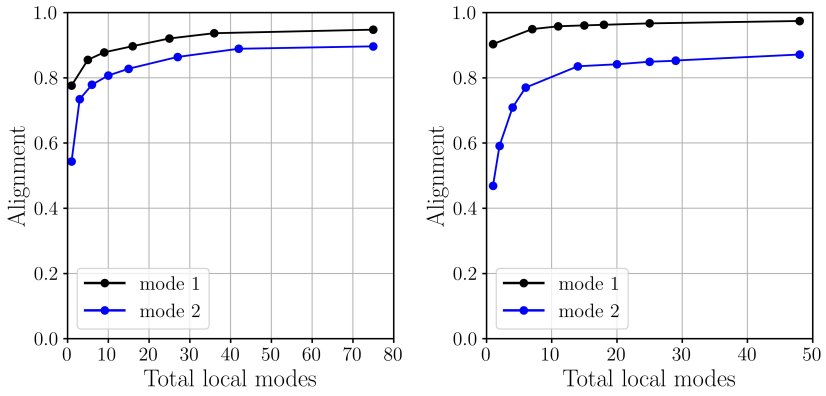

(a) $St = 0.20$ **(b) $St = 0.60$**

Fig. 5 Alignment versus the number of localized modes in reconstructing the SPOD modes 1 and 2 at $m = 0$.

growth near the nozzle. In figure 7, the localized modes are shown to initially reconstruct the double-wavepacket separately. The most amplified localized mode is shown to first model purely the downstream wavepacket of the SPOD mode by a mode 1 forcing dominated at $x/D < 10$. As for the second and third localized modes, they predict the initial growth of the mode and a more spatially accurate model of the upstream wavepacket.

To demonstrate the utility over a range of frequencies, figure 8 displays the alignment of modes versus Strouhal number. Localized resolvent analysis is shown to greatly impact the reconstruction of SPOD modes at low frequencies for mode 1. As for the subdominant modes, the localized resolvent analysis greatly improves the alignment with SPOD modes across all frequencies investigated. The localized reconstructions using least squares regression present the upper bound of the localized resolvent accuracy using all available localized modes. The number of localized modes used in the LASSO regression is presented in figure 8c where the max number of localized modes employed is 10 for all reconstructions, showing that a low number of localized modes are needed for the improvement of resolvent modes. These results are consistent with previous studies that showed the global resolvent modes accurately capture the dominant/subdominant SPOD modes at higher frequencies (KH mode frequencies), but at lower frequencies (Orr

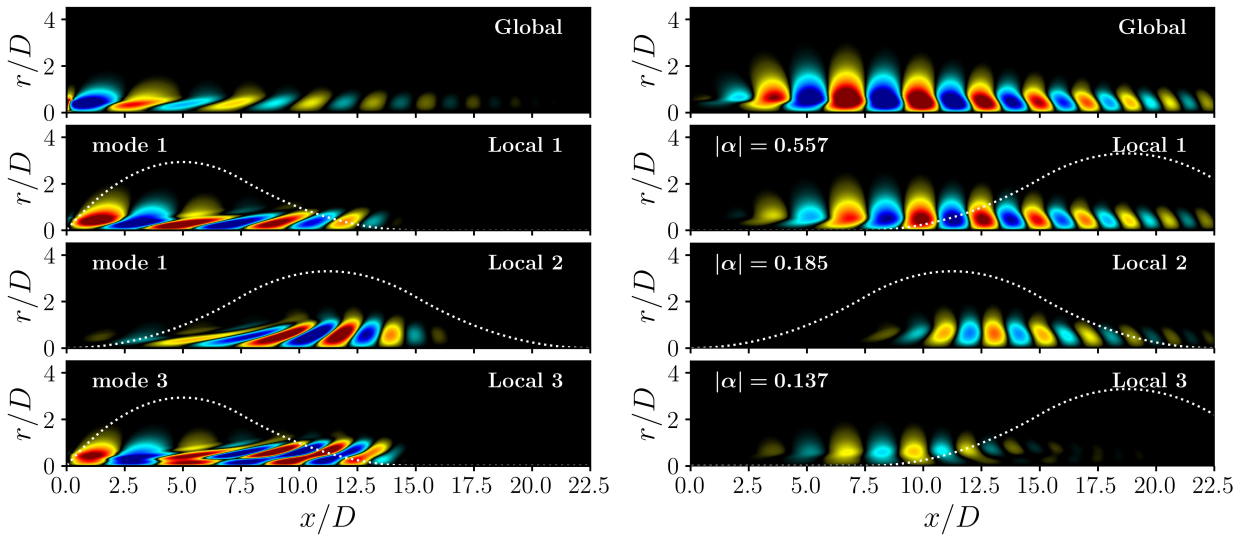

(a) Forcing modes **(b) Response modes**

Fig. 6 Individual components of SPOD mode 1 reconstruction. Shown are the radial velocity forcing and response components of the 3 highest amplified localized modes used in the reconstruction of a Mach 0.4 jet for $m = 0$ and $St = 0.20$ SPOD mode and the corresponding global mode. The response modes are plotted with respect to their amplification coefficient, α, where all response contour limits are $\pm 0.5|\psi|_\infty$ of the global mode.

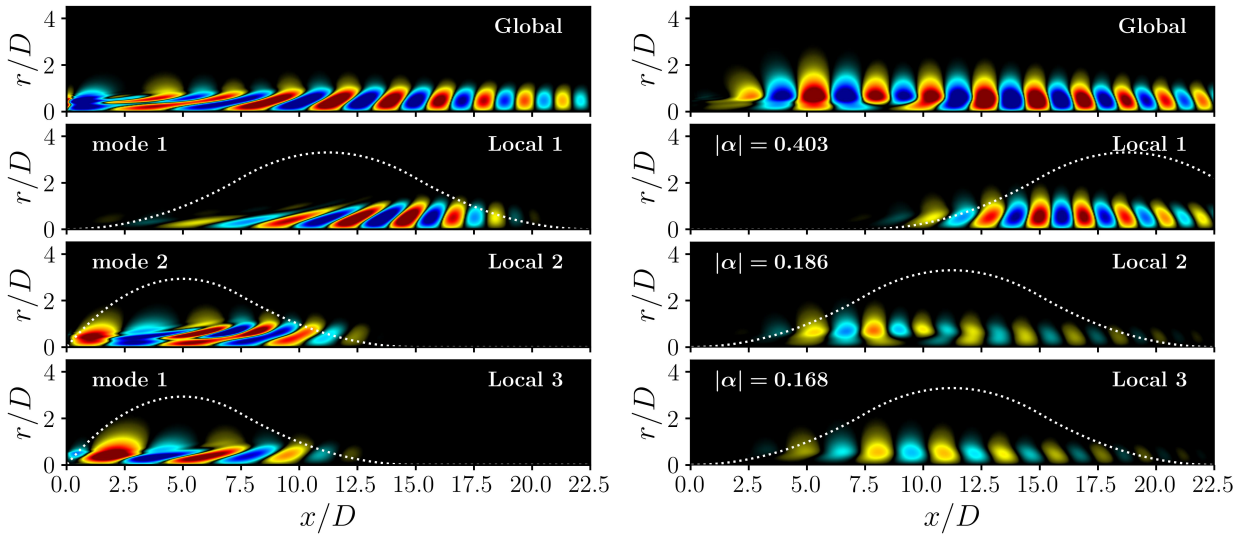

(a) Forcing modes **(b) Response modes**

Fig. 7 Individual components of SPOD mode 2 reconstruction. Shown are the radial velocity forcing and response components of the 3 highest amplified localized modes used in the reconstruction of a Mach 0.4 jet for $m = 0$ and $St = 0.20$ SPOD mode and the corresponding global mode. The response modes are plotted with respect to their amplification coefficient, α, where all response contour limits are $\pm 0.5|\psi|_\infty$ of the global mode.

mechanism frequencies), there is increasing misalignment between the resolvent and SPOD modes. On the other hand, just a few localized modes can accurately represent the SPOD modes at these low frequencies.

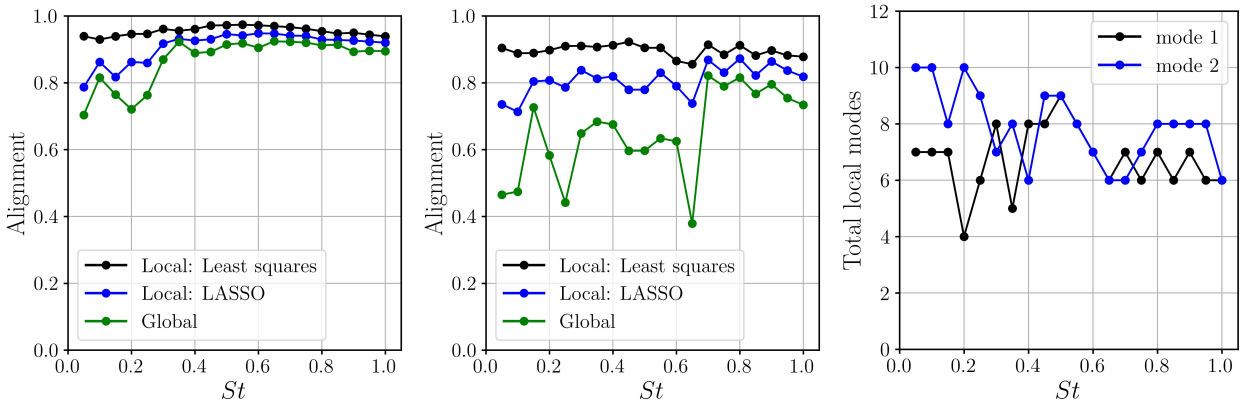

(a) Mode 1: Alignment vs. *St* **(b) Mode 2: Alignment vs. *St*** **(c) Number of localized modes in LASSO regression**

Fig. 8 Comparison of alignment versus Strouhal number at $m = 0$ between global resolvent and localized resolvent optimized using LASSO and least squares minimization.

B. Reconstruction of second-order statistics

The second-order statistics of interest are the turbulent kinetic energy and the Reynolds stresses since these quantities are easily obtained through RANS simulations. The *true* second-order statistics were computed using the LES snapshots discussed in section III.A. For the reconstruction, 13 different Strouhal numbers were used, ranging from $St = 0.01$ to $St = 1.00$, in addition to a total of 3 azimuthal wave numbers $m = (0, 1, 2)$. As for the localized reconstruction, the 3 most dominant modes are used, leading to a total of 5832 localized parameters. It's important to note that the localized modes utilized in the SPOD reconstruction are identical to those employed in the subsequent analysis. The total number of global modes at each azimuthal wave and Strouhal number is calculated to have a similar number of degrees of freedom as the localized case, which ranges from 13 to 20 subdominant modes, resulting in a total of 5517 global parameters. Each reconstruction is performed using LASSO regression where the L_2 relative error norm, E, is the new metric used to analyze the accuracy. We define the L_2 relative norm as $E = \frac{\|\boldsymbol{\Psi}-\boldsymbol{U}\|_W}{\|\boldsymbol{\Psi}\|_W}$, where $\boldsymbol{\Psi}$ is the true statistic, $\boldsymbol{U}$ is the reconstruction, and W is the Chu energy norm.

We first investigate the reconstruction of TKE using localized and global modes. Figure 9 showcases the outcome of this reconstruction, achieving a reported error of 5%. A total of 87 localized modes and 229 global modes were utilized to attain this level of accuracy, demonstrating that over 2.5 times more global modes are required for the reconstruction. It is shown in figure 10 that, as expected, the majority of the weights are at the low-frequency modes. Notably, the global weights exhibit a distinct peak at $St = 1.0$. The reconstruction, which is dominated by the low-frequency modes, results in an error localized at the high-frequency dominated near nozzle region.

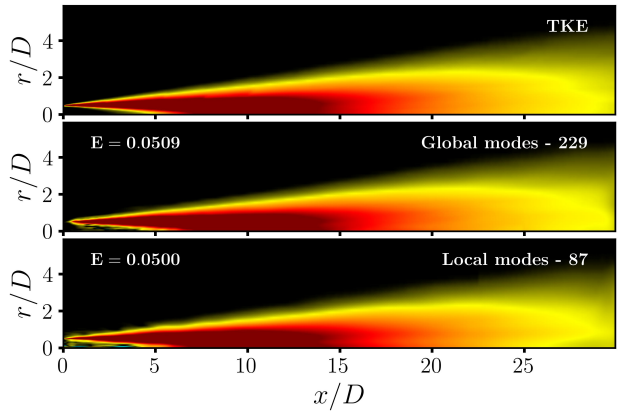

Fig. 9 TKE reconstruction with 5% error

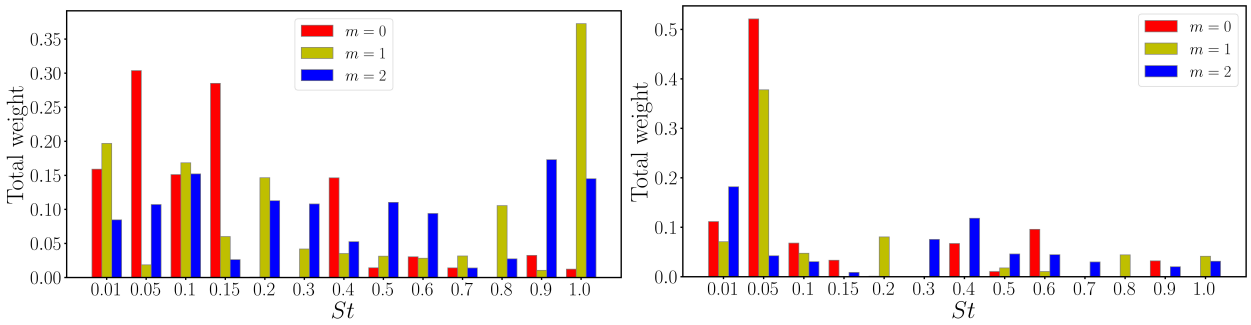

(a) Global TKE weights **(b) Local TKE weights**

Fig. 10 Total absolute weights for TKE reconstruction with 5% error

Next, the reconstruction of the Reynolds stresses is presented in figure 11. It is important to note that the 6 unique Reynolds stresses are reconstructed simultaneously (represented by components of the vector, $\mathbf{\Phi}$). The reported error represents the total error of all six stresses. In the figure, we display the axial and shear stress using both localized and global reconstructions with a target 5% error. It was found that the global reconstruction requires three times more modes than the localized one. The frequency and azimuthal content of the modes used in the fitting are plotted in figure 12, and shows similar results to the TKE reconstruction.

We also examined the other components of Reynolds stress not shown in the plot. For the jet, the Reynolds stresses $\langle u_r u_\theta \rangle$ and $\langle u_\theta u_x \rangle$ are statistically zero; the reconstructions are not, of course, identically zero, but are zero to the same accuracy as which the other Reynolds stresses match their nonzero target values.

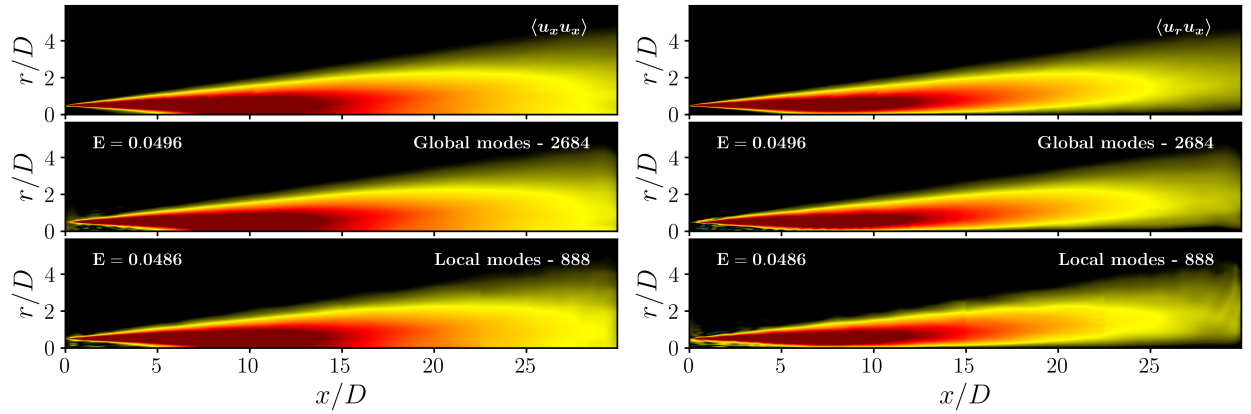

(a) Axial stress, $\langle u_x u_x \rangle$, reconstruction with 5% error **(b) Shear stress, $\langle u_x u_r \rangle$, reconstruction with 5% error**

Fig. 11 Local and global reconstruction of the Reynolds stresses with 5% error

When examining the modeling of these second-order statistics across different error ranges, the advantage of localized resolvent modes becomes clearer. Figure 13 shows the total modes required to achieve various error levels, comparing the global and localized models. At high errors, both models are shown to require a similar number of modes in the reconstruction. However, as the error decreases, the number of global modes required increases relative to the number of localized modes. This suggests that the first few dominant localized modes better represent the structures compared to the subdominant global modes.

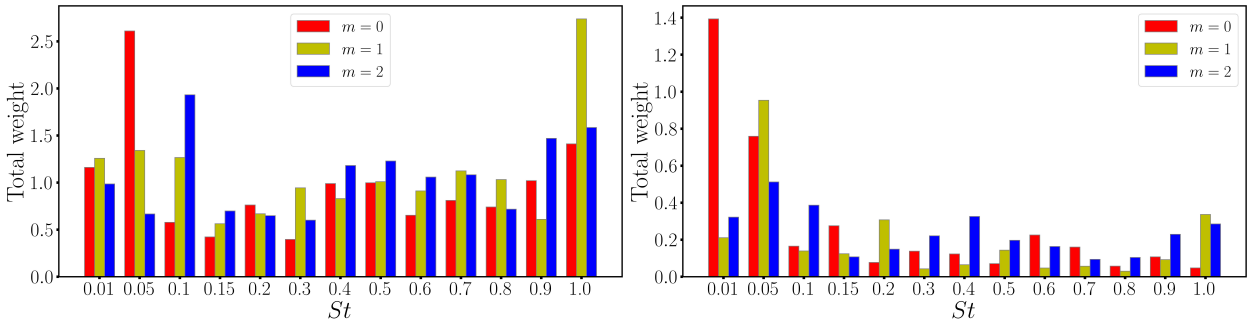

(a) Global Reynolds stress weights **(b) Localized Reynolds stress weights**

Fig. 12 Total absolute weights for Reynolds stress reconstruction with 5% error

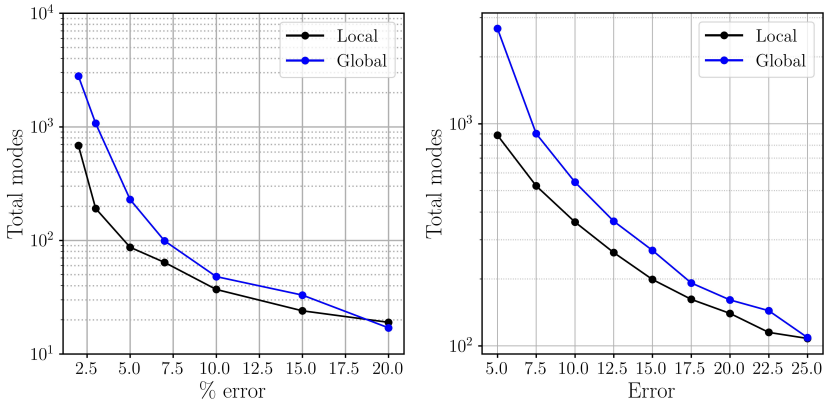

(a) TKE **(b) Reynolds Stresses**

Fig. 13 Comparison between the total number of localized and global modes used in the reconstruction of Reynolds stresses and TKE for a given error

IV. Conclusion

We developed a localized resolvent framework that adds flexibility and robustness in describing the turbulent structures in round turbulent jets. The framework consists of partitioning the computation domain of the jet into local, overlapping regions constructed by splines. Each resolvent mode is a global mode that maximizes gain between inputs and observations in the restricted regions. This new resolvent basis provides a computational compromise between an LES description and global resolvent models. To showcase the localized resolvent method, the framework was applied to LES data from a turbulent jet. The jet computational domain is divided into 6 streamwise regions, and the resulting localized modes are assessed in their ability to reconstruct (i) global SPOD modes and (ii) Reynolds stresses and TKE. The reconstructions are compared to that of the global resolvent response with RANS-based eddy-viscosity field [4]. The localized framework was shown to greatly improve the modeling of SPOD modes with a minimal number of localized modes, predominately for the most dominant modes at low frequencies and all frequencies for subdominant modes. By breaking down the optimization and displaying the most amplified localized modes, we see that the first few modes construct the general shape of the SPOD response. Then, each additional localized mode starts modeling the different complex localized mode shapes found throughout the model. At the low frequencies, the reconstruction was shown to greatly improve the prediction up until about 20 localized modes. However, beyond this threshold, the model tends to overfit and reconstruct the distorted structures present in the SPOD modes, as evidenced by the least squares reconstruction.

The second case presented was the comparison between modeling second-order statistics using localized and global resolvent modes. The second-order statistics modeled were the TKE and the 6 unique Reynolds stresses. It was found

that the number of global modes compared to localized modes exponentially increased with decreasing error. For each reconstruction, each model favored the low-frequency modes, and the weight of the high-frequency components increased with decreasing error. Consequently, this resulted in an error localized in the near nozzle region.

Overall, localized resolvent analysis offers a more flexible and robust basis than global resolvent analysis. It is worth noting that our pursuit of a data-driven model extends beyond the reconstruction of SPOD modes to encompass a wide range of outputs. By efficiently using localized modes to accurately model second-order statistics, we have established an initial relationship between localized resolvent modes and RANS quantities, crucial for the development of the proposed data-driven method. Further analysis is required to elucidate the insights these reconstructions provide regarding computing optimized global quantities.

Acknowledgments

This work has been supported by the Office of Naval Research under grant N00014-23-1-2650 and the Federal Aviation Administration under grant 13-C-AJFE-UI. The main LES calculations were carried out on CRAY XE6 machines at DoD HPC facilities in ERDC DSRC.

References

[1] Lumley, J. L., "The structure of inhomogeneous turbulent flows," *Atmospheric turbulence and radio wave propagation*, 1967.

[2] McKeon, B. J., and Sharma, A. S., "A critical-layer framework for turbulent pipe flow," *Journal of Fluid Mechanics*, Vol. 658, 2010, p. 336–382. https://doi.org/10.1017/S002211201000176X.

[3] Schmidt, O. T., Towne, A., Rigas, G., Colonius, T., and Brès, G. A., "Spectral analysis of jet turbulence," *Journal of Fluid Mechanics*, Vol. 855, 2018, p. 953–982. https://doi.org/10.1017/jfm.2018.675.

[4] Pickering, E., Rigas, G., Schmidt, O. T., Sipp, D., and Colonius, T., "Optimal eddy viscosity for resolvent-based models of coherent structures in turbulent jets," *Journal of Fluid Mechanics*, Vol. 917, 2021, p. A29.

[5] Towne, A., Schmidt, O. T., and Colonius, T., "Spectral proper orthogonal decomposition and its relationship to dynamic mode decomposition and resolvent analysis," *Journal of Fluid Mechanics*, Vol. 847, 2018, p. 821–867. https://doi.org/10.1017/jfm.2018.283.

[6] Garnaud, X., Lesshafft, L., Schmid, P. J., and Huerre, P., "The preferred mode of incompressible jets: linear frequency response analysis," *Journal of Fluid Mechanics*, Vol. 716, 2013, p. 189–202. https://doi.org/10.1017/jfm.2012.540.

[7] Jeun, J., Nichols, J. W., and Jovanović, M. R., "Input-output analysis of high-speed axisymmetric isothermal jet noise," *Physics of Fluids*, Vol. 28, No. 4, 2016, p. 047101. https://doi.org/10.1063/1.4946886, URL https://doi.org/10.1063/1.4946886.

[8] Lighthill, M. J., "On sound generated aerodynamically I. General theory," *Proceedings of the Royal Society of London. Series A. Mathematical and Physical Sciences*, Vol. 211, No. 1107, 1952, pp. 564–587.

[9] GOLDSTEIN, M. E., "A generalized acoustic analogy," *Journal of Fluid Mechanics*, Vol. 488, 2003, p. 315–333. https://doi.org/10.1017/S0022112003004890.

[10] Pickering, E. M., Towne, A., Jordan, P., and Colonius, T., "Resolvent-based jet noise models: a projection approach," *AIAA Scitech 2020 Forum*, 2020, p. 0999.

[11] Pickering, E., Towne, A., Jordan, P., and Colonius, T., "Resolvent-based modeling of turbulent jet noise," *The Journal of the Acoustical Society of America*, Vol. 150, No. 4, 2021, pp. 2421–2433.

[12] Karban, U., Bugeat, B., Towne, A., Lesshafft, L., Agarwal, A., and Jordan, P., "An empirical model of noise sources in subsonic jets," *Journal of Fluid Mechanics*, Vol. 965, 2023, p. A18.

[13] Bugeat, B., Karban, U., Agarwal, A., Lesshafft, L., and Jordan, P., "Resolvent modelling of jet noise: the need for forcing models," 2023.

[14] Morra, P., Semeraro, O., Henningson, D. S., and Cossu, C., "On the relevance of Reynolds stresses in resolvent analyses of turbulent wall-bounded flows," *Journal of Fluid Mechanics*, Vol. 867, 2019, p. 969–984. https://doi.org/10.1017/jfm.2019.196.

[15] Towne, A., Lozano-Durán, A., and Yang, X., "Resolvent-based estimation of space–time flow statistics," *Journal of Fluid Mechanics*, Vol. 883, 2020, p. A17. https://doi.org/10.1017/jfm.2019.854.

[16] Gómez, F., Blackburn, H. M., Rudman, M., Sharma, A. S., and McKeon, B. J., "A reduced-order model of three-dimensional unsteady flow in a cavity based on the resolvent operator," *Journal of Fluid Mechanics*, Vol. 798, 2016, p. R2. https://doi.org/10.1017/jfm.2016.339.

[17] Beneddine, S., Sipp, D., Arnault, A., Dandois, J., and Lesshafft, L., "Conditions for validity of mean flow stability analysis," *Journal of Fluid Mechanics*, Vol. 798, 2016, p. 485–504. https://doi.org/10.1017/jfm.2016.331.

[18] Chu, B.-T., "On the energy transfer to small disturbances in fluid flow (Part I)," *Acta Mechanica*, Vol. 1, No. 3, 1965, p. 215–234. https://doi.org/10.1007/bf01387235, URL http://dx.doi.org/10.1007/BF01387235.

[19] Heidt, L., Colonius, T., Nekkanti, A., Schmdit, O., Maia, I., and Jordan, P., "Analysis of forced subsonic jets using spectral proper orthogonal decomposition and resolvent analysis," *AIAA Aviation 2021 Forum*, 2021, p. 2108.

[20] Welch, P., "The use of fast Fourier transform for the estimation of power spectra: A method based on time averaging over short, modified periodograms," *IEEE Transactions on Audio and Electroacoustics*, Vol. 15, No. 2, 1967, p. 70–73. https://doi.org/10.1109/tau.1967.1161901, URL http://dx.doi.org/10.1109/TAU.1967.1161901.

[21] Heidt, L., and Colonius, T., "Optimal frequency resolution for spectral proper orthogonal decomposition," *arXiv preprint arXiv:2402.15775*, 2024.

[22] Brès, G. A., Bose, S. T., Ham, F., and Lele, S. K., "Unstructured Large Eddy Simulations for Nozzle Interior Flow Modeling and Jet Noise Predictions," *20th AIAA/CEAS Aeroacoustics Conference*, American Institute of Aeronautics and Astronautics, 2014. https://doi.org/10.2514/6.2014-2601, URL http://dx.doi.org/10.2514/6.2014-2601.

[23] Brès, G. A., Ham, F. E., Nichols, J. W., and Lele, S. K., "Unstructured Large-Eddy Simulations of Supersonic Jets," *AIAA Journal*, Vol. 55, No. 4, 2017, pp. 1164–1184. https://doi.org/10.2514/1.J055084, URL https://doi.org/10.2514/1.J055084.

[24] Brès, G. A., Jordan, P., Jaunet, V., Le Rallic, M., Cavalieri, A. V. G., Towne, A., Lele, S. K., Colonius, T., and Schmidt, O. T., "Importance of the nozzle-exit boundary-layer state in subsonic turbulent jets," *Journal of Fluid Mechanics*, Vol. 851, 2018, p. 83–124. https://doi.org/10.1017/jfm.2018.476.

Technical Report Documentation Page

1. Report No.	2. Government Accession No.	3. Recipient's Catalog No.
AIAA 2024-3205		

4. Title and Subtitle	5. Report Date
Localized resolvent-mode bases for turbulence statistics	June 2024
	6. Performing Organization Code

7. Author(s)	8. Performing Organization Report No.
Ethan Eichberger, Liam Heidt and Tim Colonius	

9. Performing Organization Name and Address	10. Work Unit No. (TRAIS)
Center of Excellence for: Alternative Jet Fuels and Environment University of Illinois Urbana-Champaign, Urbana, IL 61801	11. Contract or Grant No. 13-C-AJFE-UI-031

12. Sponsoring Agency Name and Address	13. Type of Report and Period Covered
Federal Aviation Administration Office of Environment and Energy	Conference Proceedings
	14. Sponsoring Agency Code

15. Supplementary Notes

https://authors.library.caltech.edu/records/w1hg5-p4454
https://authors.library.caltech.edu/records/w1hg5-p4454/files/eichberger-et-al-2024-localized-resolvent-mode-bases-for-turbulence-statistics.pdf?download=1

16. Abstract

Modes from global resolvent analyses have been shown to accurately model the frequencies and spatial structure of the dominant coherent structures in several turbulent flows. However, resolvent-mode forcing models must be developed to predict the amplitude of the structures or other flow statistics, including the radiated noise. The present research aims to apply data-driven approaches to learn forcing coefficients from lower-order statistics available from Reynolds-averaged Navier-Stokes (RANS) predictions. As a first step towards this goal, we present a novel localized resolvent framework that reconstructs global quantities at low rank through spatially restricting the resolvent forcing and response domains. To illustrate the flexibility and robustness of the proposed framework, we initially utilize localized resolvent modes to reconstruct the spectral proper orthogonal decomposition (SPOD) modes of an isothermal Mach 0.4 jet at • Ł Ł 450, 000. The results showcase the flexibility localized resolvent modes provide in the construction of global SPOD, while using 10 or fewer total localized modes total across • Ł Ł [0.05, 1.00]. Furthermore, we employ localized resolvent modes to reconstruct second-order statistics, comparing their performance with that of global modes. At low reconstruction error, it is shown that about twice as many global modes are needed to achieve comparable errors.

17. Key Words	18. Distribution Statement
ASCENT	

19. Security Classif. (of this report)	20. Security Classif. (of this page)	21. No. of Pages	22. Price
Unclassified	Unclassified		